J. Fluid Mech. (2011), *vol.* 686, *pp.* 507–533.
doi:10.1017/jfm.2011.342

Large-eddy simulation of the zero-pressure-gradient turbulent boundary layer up to $Re_\theta = O(10^{12})$

M. Inoue† and D. I. Pullin

Graduate Aerospace Laboratories, 205-45, California Institute of Technology, Pasadena, CA 91125, USA

(Received 14 February 2011; revised 5 August 2011; accepted 7 August 2011;
first published online 29 September 2011)

A near-wall subgrid-scale (SGS) model is used to perform large-eddy simulation (LES) of the developing, smooth-wall, zero-pressure-gradient flat-plate turbulent boundary layer. In this model, the stretched-vortex, SGS closure is utilized in conjunction with a tailored, near-wall model designed to incorporate anisotropic vorticity scales in the presence of the wall. Large-eddy simulations of the turbulent boundary layer are reported at Reynolds numbers Re_θ based on the free-stream velocity and the momentum thickness in the range $Re_\theta = 10^3$–10^{12}. Results include the inverse square-root skin-friction coefficient, $\sqrt{2/C_f}$, velocity profiles, the shape factor H, the von Kármán 'constant' and the Coles wake factor as functions of Re_θ. Comparisons with some direct numerical simulation (DNS) and experiment are made including turbulent intensity data from atmospheric-layer measurements at $Re_\theta = O(10^6)$. At extremely large Re_θ, the empirical Coles–Fernholz relation for skin-friction coefficient provides a reasonable representation of the LES predictions. While the present LES methodology cannot probe the structure of the near-wall region, the present results show turbulence intensities that scale on the wall-friction velocity and on the Clauser length scale over almost all of the outer boundary layer. It is argued that LES is suggestive of the asymptotic, infinite Reynolds number limit for the smooth-wall turbulent boundary layer and different ways in which this limit can be approached are discussed. The maximum Re_θ of the present simulations appears to be limited by machine precision and it is speculated, but not demonstrated, that even larger Re_θ could be achieved with quad- or higher-precision arithmetic.

Key words: turbulence modelling, turbulence simulation, turbulent boundary layers

1. Introduction

Numerical resolution requirements limit applicability of direct numerical simulation (DNS) to turbulent flows at low to moderate Reynolds numbers. In DNS of incompressible flows, a wide range of dynamically important scales of motion must be resolved, including the smallest dissipative Kolmogorov scales. Large-eddy simulation (LES) is now a viable alternative to DNS and experiment (Jiménez 2003). Here, only the large scales of motion are resolved while the effects of small unresolved eddies are modelled; this enterprise is referred to as SGS modelling. In LES, this takes the form

† Email address for correspondence: minoue@caltech.edu

of closures for the subgrid contributions to the fluxes of momentum, energy and scalar transport insofar as these appear in the LES equations for the resolved scales. LES has had a significant impact on the development of turbulence prediction techniques, and many different approaches have been developed; see Lesieur & Metais (1996), Meneveau & Katz (2000) and Sagaut (2002) for reviews.

Direct numerical simulation of the spatially developing, smooth-wall turbulent boundary has hitherto been limited to $Re_\theta = 3\text{–}5 \times 10^3$ (see Schlatter & Örlü 2010), while laboratory experiments and surface layer experiments have reached values ten to one thousand times larger (Österlund 1999; DeGraaff & Eaton 2000; Metzger, McKeon & Holmes 2007; Mathis, Hutchins & Marusic 2009). The LES of wall-bounded flow at both laboratory and atmospheric-layer Reynolds numbers remains a significant challenge (e.g. Cabot & Moin 1999; Moin 2002; Piomelli & Balaras 2002; Templeton, Medic & Kalitzin 2005; Piomelli 2008), because close to the wall the paradigm of flow dominance by large scales fails (Pope 2004). Near-wall motions are highly anisotropic and their spatial extent and structure are determined by complex near-wall dynamics conditioned by streamwise vortices streaks and possibly other structures. These scales probably dominate the transport dynamics but will tend to be under-resolved at moderate grid resolution and large Re_θ. One approach is near-wall resolved LES where the LES grid extends into the viscous layer, providing partial resolution of the viscous wall length in at least the wall-normal direction, while LES operates in the outer part of the boundary layer. This has been shown to work well at moderate Reynolds numbers (Schlatter *et al.* 2010) but the cost scales approximately as Reynolds number to the power 1.8 (see Pope 2000), which may limit application at large Re_θ. An alternative is near-wall modelling, which attempts to eliminate the near-wall layer from the overall LES (Piomelli 2008). Some means is then required, first, of providing boundary conditions for the large-eddy simulations that replace the usual no-slip condition used for the Navier–Stokes equations, and second, of accurately determining the wall shear stress, or equivalently, the wall-friction velocity at the bottom of a region that is not resolved.

Wall modelling has also been used for LES of the atmospheric boundary layer using so-called 'wall-stress boundary conditions' that relate a wall shear stress, sometimes determined from an assumed log law, to the velocity at the first grid point from the wall (Porté-Agel, Meneveau & Parlange 2000; Lu & Porté-Agel 2010; Anderson & Meneveau 2011). Wall-stress models appear in a variety of implementations, and since the present wall model is not of this type, the reader is referred to a review (Piomelli 2008) for technical details. Using a specified wall roughness scale, these methods provide LES for effective rough-wall flow at nominally large but undetermined Reynolds numbers.

Wall models based on either a table look-up, using a universal mean velocity profile to determine the friction velocity (Templeton *et al.* 2005), or on a wall-boundary condition using optimal control theory coupled to a Reynolds-averaged Navier–Stokes model (Templeton, Wang & Moin 2008), have enabled LES of streamwise periodic, smooth-wall channel flow up to $Re_\tau = O(10^4)$. These atmospheric and smooth-wall channel-flow large-eddy simulations provide reasonable representations of the mean log-like velocity profile at either unknown or moderately large Reynolds number but do not appear to have yet been used to systematically study the spatially developing, zero-pressure-gradient boundary layer at either large laboratory Reynolds numbers (Österlund 1999; DeGraaff & Eaton 2000; Mathis *et al.* 2009) or extreme Reynolds numbers typical of field experiments in the atmospheric surface layer (Metzger *et al.* 2007). Such simulations must dynamically calculate the streamwise-

varying skin-friction velocity in relation to the free-stream velocity, while using a wall model enabling resolution of quantities that may exhibit weak but definite Reynolds number dependence or perhaps Reynolds number independence. For smooth-wall flow, examples of the former are the streamwise velocity-profile shape factor and the skin-friction coefficient, while examples of the latter are the Coles wake factor and possibly the von Kármán constant. This is a regime that, to date, has proved inaccessible to direct numerical simulation. It is the main focus of the present work.

Chung & Pullin (2009) developed an SGS model tailored to smooth wall-bounded flow by attempting to incorporate widely accepted elements of near-wall vortices into a structure-based wall model. Their approach begins by averaging the streamwise momentum equation over a thin layer adjacent to the wall. Using inner-scaling for the unsteady term of the averaged equation while coupling other terms to the outer LES, they obtained an ordinary differential equation (ODE) for the local wall-normal velocity gradient, or equivalently, the wall-friction velocity. This is solved as an auxiliary equation for the main, outer-flow LES and provides a direct calculation of the friction velocity. The boundary condition for the outer LES is applied at a raised or 'virtual wall' by integrating, in the the wall-normal direction, the stretched-vortex SGS model expression for the wall-normal transport of streamwise momentum, under the assumption that there exists, in the near-wall layer, a hierarchy of streamwise vortices whose size scales with distance from the wall (see Nickels *et al.* 2007). This gives a log-like relation for the mean streamwise velocity that, in conjunction with the wall-friction velocity obtained from the wall-layer ODE, provides a slip velocity for the outer LES. The model also gives a means of determining a Kármán-like constant dynamically. Chung & Pullin (2009) applied the model to LES of channel flow up to $Re_\tau = 2\times 10^7$, while Chung & McKeon (2010) performed LES of large-scale structures in turbulent flow in long channels.

Here this model is extended to the LES of the zero-pressure-gradient, flat-plate turbulent boundary layer (ZPGFPTBL). In § 2 the present SGS wall model is described. A brief account of previous numerical simulations of the ZPGFPTBL is given in § 3. This is followed in § 4 by a description of the numerical method and boundary conditions used here. The results of the present LES over a wide range of Reynolds numbers are described in detail in § 5, while some conclusions and scenarios suggested by the LES are discussed in §§ 6 and 7.

2. Subgrid-scale model for wall-bounded flow

We now briefly describe the SGS model: for details see Chung & Pullin (2009). In the following, x_1 or x is the streamwise coordinate, x_2 or y is the spanwise coordinate, and x_3 or z is the wall-normal coordinate. The generically filtered Navier–Stokes equations with filter scale Δ_c are

$$\frac{\partial \widetilde{u}_i}{\partial t} + \frac{\partial \widetilde{u}_i\widetilde{u}_j}{\partial x_j} = -\frac{\partial \widetilde{p}}{\partial x_i} + \nu\frac{\partial^2 \widetilde{u}_i}{\partial x_j^2} - \frac{\partial T_{ij}}{\partial x_j}, \quad \frac{\partial \widetilde{u}_i}{\partial x_i} = 0, \tag{2.1}$$

where $\widetilde{u}_i$ is the filtered velocity, $T_{ij} = \widetilde{u_iu_j} - \widetilde{u}_i\widetilde{u}_j = \widetilde{\widetilde{u}_iu_j'} + \widetilde{u_i'\widetilde{u}_j} + \widetilde{u_i'u_j'}$ is the subgrid stress tensor, ν is the kinematic viscosity and p is pressure divided by density.

2.1. *The stretched-vortex SGS model*

It is assumed that, embedded within each computational cell, there exists a superposition of stretched vortices, each having orientation taken from a delta-function probability density function (p.d.f.) that is either prescribed or dynamic (Misra &

Pullin 1997). In the simplest version, used here, a single active subgrid vortex is aligned with the unit vector $\boldsymbol{e}^v$, with resulting subgrid stress tensor

$$T_{ij} = (\delta_{ij} - e_i^v e_j^v)K, \quad K = \int_{k_c}^{\infty} E(k)\,\mathrm{d}k, \tag{2.2}$$

where K is the subgrid kinetic energy. The cutoff wavenumber is $k_c = \pi/\Delta_c$, $\Delta_c = (\Delta_x\,\Delta_y\,\Delta_z)^{1/3}$, and $E(k)$ is the SGS energy spectrum. The latter is obtained by supposing that the SGS vortices are of the stretched spiral type, which have energy spectra (Lundgren 1982)

$$E(k) = \mathscr{K}_0 \epsilon^{2/3} k^{-5/3} \exp\left[-2k^2\nu/(3|\widetilde{a}|)\right], \tag{2.3}$$

where $\widetilde{a} = e_i^v e_j^v \widetilde{S}_{ij}$, the stretching felt along the subgrid vortex axis imposed by the resolved scales, and $\widetilde{S}_{ij} = (1/2)\,(\partial\widetilde{u}_i/\partial x_j + \partial\widetilde{u}_j/\partial x_i)$ is the resolved strain-rate tensor. Combining the second equation of (2.2) and (2.3) gives

$$\left.\begin{aligned} K &= \tfrac{1}{2}\,\mathscr{K}_0'\,\Gamma\left[-1/3, \kappa_c^2\right], \quad \mathscr{K}_0' = \mathscr{K}_0\epsilon^{2/3}\lambda_v^{2/3}, \\ \lambda_v &= (2\nu/3|\widetilde{a}|)^{1/2}, \quad \kappa_c = k_c\lambda_v, \end{aligned}\right\} \tag{2.4}$$

and Γ is the incomplete gamma function. Here $\boldsymbol{e}^v$ is aligned with the principal extensional eigenvector of the resolved-scale strain-rate tensor except at the wall (see § 2.3). We note that $\boldsymbol{e}^v$ can be a discontinuous function of S_{ij} when the most extensional and intermediate eigenvalues exchange. Our experience is that the spatial measure of this is negligible and has no effect on the LES. The parameter $\mathscr{K}_0\epsilon^{2/3}$ is obtained dynamically by structure-function matching at the grid-scale cutoff (Pullin & Chan 2000; Chung & Pullin 2009).

Chung & Pullin (2009) extended (2.2) to incorporate transport of resolved-scale axial velocity, modelled as a passive scalar, by SGS vortices (Pullin 2000; Pullin & Lundgren 2001; O'Gorman & Pullin 2003; Chung & Pullin 2009)

$$\begin{aligned} T_{ij} &\equiv \widetilde{u_i'u_j'} + \widetilde{u_i'}\widetilde{u}_j + \widetilde{u}_i\widetilde{u_j'} \\ &= K(\delta_{ij} - e_i^v e_j^v) - K_s\left[e_j^v e_k^v \frac{\partial\widetilde{u}_k}{\partial x_l}(\delta_{li} - e_l^v e_i^v) + e_i^v e_k^v \frac{\partial\widetilde{u}_k}{\partial x_l}(\delta_{lj} - e_l^v e_j^v)\right], \end{aligned} \tag{2.5}$$

where $2\,K_s = \gamma\,\Delta_c\,K^{1/2}$ and γ is a momentum mixing constant to be discussed below.

2.2. *The wall shear stress*

The main idea is to integrate across the near-wall layer in a way that models the appropriate physics and recognizes anisotropy while providing a slip boundary condition at a raised virtual wall for the resolved-scale LES (Chung & Pullin 2009). With the physical wall at $z = 0$, we apply to the streamwise momentum equation an xy-plane filter '$\widetilde{\ }$' and a top-hat, or averaging wall-normal filter

$$\langle\phi\rangle(x, y, t) \equiv \frac{1}{h}\int_0^h \widetilde{\phi}(x, y, z, t)\,\mathrm{d}z, \tag{2.6}$$

over a wall-adjacent layer of height h, to obtain

$$\frac{\partial\langle u\rangle}{\partial t} + \frac{\partial\langle uu\rangle}{\partial x} + \frac{\partial\langle uv\rangle}{\partial y} = -\frac{1}{h}\widetilde{uw}\Big|_h - \frac{\partial\widetilde{p}}{\partial x}\bigg|_h + \frac{\nu}{h}\left(\frac{\partial\widetilde{u}}{\partial z}\bigg|_h - \eta_0\right), \tag{2.7}$$

where we have used the wall boundary condition $\widetilde{u}(x, y, 0, t) = 0$ and have neglected lateral diffusion. The local wall-normal velocity gradient is

$$\eta_0(x, y, t) \equiv \left(\frac{\partial \widetilde{u}}{\partial z}\right)_{z=0}. \tag{2.8}$$

The local wall shear stress is $\tau_0(x, y, t)/\rho = \nu\eta_0(x, y, t) \equiv u_\tau^2(x, y, t)$, where u_τ is the wall-friction velocity and the viscous wall unit is $l^+ \equiv \nu/u_\tau$.

Equation (2.7) can be reduced to an ODE for the wall-normal velocity gradient η_0 by using a local inner-scaling ansatz of the form

$$\widetilde{u}(x, y, z, t) = (\nu\eta_0(x, y, t))^{1/2} F(z^+), \quad z^+ = z(\eta_0(x, y, t)/\nu)^{1/2} \equiv z/l^+ \tag{2.9}$$

applied to the unsteady term only, and by approximating the x and y convective terms by their value at the top of the integrated wall layer $z = h$, with the result (Chung & Pullin 2009)

$$\frac{\partial \eta_0}{\partial t} = \frac{2\eta_0}{\widetilde{u}|_h}\left[-\frac{1}{h}\widetilde{uw}\Big|_h - \frac{\partial \widetilde{uu}|_h}{\partial x} - \frac{\partial \widetilde{uv}|_h}{\partial y} - \frac{\partial \widetilde{p}}{\partial x}\Big|_h + \frac{\nu}{h}\left(\frac{\partial \widetilde{u}}{\partial z}\Big|_h - \eta_0\right)\right]. \tag{2.10}$$

Owing to a cancellation of two integrals arising from the wall-normal integration, the specific form of $F(z^+)$ in $0 \leqslant z < h$ does not appear in (2.10).

In the LES, (2.10) is an auxiliary equation to determine the evolution of u_τ. For the present staggered-grid numerical method, we set $h = h_0 + \Delta_z/2$, where h_0 is the wall-normal distance of the virtual wall from the physical wall and Δ_z is the near-wall cell size. The first grid point for the streamwise velocity component within the LES domain is at $\Delta_z/2$. The quantities on the right-hand side are determined from resolved-scale LES quantities at $z = h$. This allows determination of u_τ without resolving the near-wall steep gradients. To close this coupling, appropriate boundary conditions for the LES are required.

2.3. *Slip velocity at a raised or 'virtual' wall*

The LES takes place above a fixed, Reynolds-number-independent height, $h_0 = \alpha\,\Delta_z$, $\alpha < 1$. Chung & Pullin (2009) defined three regions near the wall (see their figure 1): (I) $0 \leqslant z \leqslant h_v$, essentially the viscous sublayer, (II) $h_v < z \leqslant h_0$, an overlap layer where the shear stress is approximately constant, and is modelled by the extended stretched-vortex SGS model consisting of attached vortices aligned with $\boldsymbol{e}_x$, and (III) $h_0 < z$, where non-universal outer-flow features are computed with LES coupled with the original stretched-vortex SGS model of detached subgrid vortices aligned with $\boldsymbol{e}_{\widetilde{S}}$. The plane $z = h_0$ is a lifted virtual wall. In region (I) we use $\widetilde{u}^+ = z^+$, where $\widetilde{u}^+ = \widetilde{u}/u_\tau$, $z^+ = z/l^+$, and u_τ is known from (2.10). In particular, $\widetilde{u}^+|_{h_v} = h_v^+$, where $h_v^+ = h_v/l^+$. For a hydrodynamically smooth wall we use the empirical value $h_v^+ \approx 10.23$ based on the intercept between the linear and log component of the law of the wall. Hence $\widetilde{u}^+|_{h_v} = h_v^+ = 10.23$. This is the only empirical constant in the present model.

Chung & Pullin (2009) derived an effective slip-velocity at the top of region (II), $h_v < z \leqslant h_0$ in a way that couples both (2.5) and (2.10). Briefly, it is assumed that in region (II) the total shear stress is approximately constant (Townsend 1976) and that near-wall vortices are streamwise aligned (see e.g. Head & Bandyopadhyay 1981; Robinson 1991) $(e_x^v, e_y^v, e_z^v) = (1, 0, 0) \Leftrightarrow \boldsymbol{e}^v = \boldsymbol{e}_x$. Substituting these into the stretched-spiral vortex extended model, (2.5), and noting that the only non-zero component of

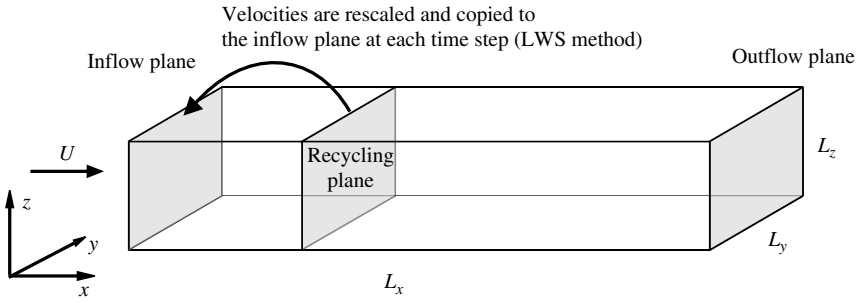

FIGURE 1. A schematic of the computational 'code-A' domain showing the recycling region.

the mean velocity gradient tensor is $\mathrm{d}\widetilde{u}/\mathrm{d}z$ then gives

$$T_{xz} = -\frac{1}{2}\gamma_{\mathrm{II}} K^{1/2} \Delta_c \frac{\mathrm{d}\widetilde{u}}{\mathrm{d}z}. \tag{2.11}$$

The physical mechanism that produces this shear stress is the action of the spiralling streamwise vortices winding the local axial velocity, now identified as the mean streamwise velocity, thereby transporting higher-momentum fluid towards the wall and transporting low-momentum fluid away from the wall.

Assuming that SGS vortices in (II) are 'attached to the wall' and that $\Delta_c = z$ (vortex size scales with wall distance (Nickels *et al.* 2007)), then $\widetilde{u}$ can be integrated within region (II) to give (Chung & Pullin 2009)

$$\widetilde{u}|_{h_0} = u_\tau \left(\frac{1}{\mathscr{K}_1} \log\left(\frac{h_0}{h_v}\right) + h_v^+ \right), \quad \mathscr{K}_1(x,y,t) = \frac{\gamma_{\mathrm{II}} K^{1/2}}{2\,(-T_{xz}/u_\tau)}, \tag{2.12}$$

where the constant of integration is chosen by putting $\widetilde{u}|_{h_v} = u_\tau\, h_v^+$. Equation (2.12) and $\widetilde{w}$ obtained from continuity give the Dirichlet boundary conditions at the lifted virtual wall h_0, where u_τ is obtained from the solution of (2.10). The parameter $\mathscr{K}_1(x,y,t)$ is an effective von Kármán constant, κ. The vertical momentum mixing constant γ_{II} is estimated by matching Townsend's structure parameter $a_1 = T_{13}/T_{ii} = T_{13}/(2K)$ at the interface of regions (II) and (III), $z = h_0$, where both inner and outer layer modelling ideas are valid, giving $\gamma_{\mathrm{II}} = 2^{1/2}/\pi \approx 0.45$ (Chung & Pullin 2009). This value is used here for all LES.

2.4. *Summary of SGS wall model*

The near-wall SGS model can be summarized as follows: for every cell adjacent to the bottom walls (2.10) is solved for η_0 with terms on the right-hand side provided by the LES at the first grid point for the streamwise velocity component. This provides $\eta_0(x,y,t)$ and thus $u_\tau(x,y,t)$. Equation (2.12) is then used to evaluate the streamwise slip velocity $\widetilde{u}|_{h_0}(x,y,t)$ at $z = h_0$, with $\mathscr{K}_1$ evaluated from the second of (2.12) with K and T_{xz} evaluated at $z = h$ from the LES structure-function-matching procedure. The other boundary conditions at $z = h_0$ are $\widetilde{v}|_{h_0}(x,y,t) = 0$, $\widetilde{w}|_{h_0}(x,y,t) = -2\,h_0\,\widetilde{u}|_{h_0}\,(\partial\eta_0/\partial x)/(2\,\eta_0)$ from wall-normal integration of continuity. This method couples the LES to the modelled, near-wall dynamics. Presently we use $h_0 = 0.18\,\Delta_z$, independent of the LES resolution, and consider this as part of the overall grid. Tests to investigate sensitivity to h_0 were performed (Chung & Pullin 2009). The near-wall SGS model provides a means of dynamically calculating

the instantaneous local 'Kármán constant', $\mathscr{K}_1$, as part of the integrated SGS-model coupled to the LES.

3. Flat-plate turbulent boundary layers: background

Research on turbulent boundary layers (TBL) has a long history. Unlike channel or pipe flow, the thickness of the turbulent zone, or TBL thickness $\delta(x)$, and the wall shear stress $\tau_w(x)$ vary with streamwise distance and are not fixed in advance by the channel height or the applied, favourable pressure gradient. They must be computed as part of the simulation. Moreover, the flow outside the TBL may be either smooth or contain free-stream turbulence, and may also contain wall-normal transpiration velocities which are related to the pressure gradient and which must be accurately represented in any simulation. Nonetheless the near-wall regions of channel/pipe flow and that of the TBL are similar, even though the scaling may not be identical (e.g. Spalart 1988; DeGraaff & Eaton 2000), which suggests that the present near-wall SGS model, which is entirely local in character including its incorporation of local pressure gradients, should be applicable at least to spatially developing equilibrium boundary layers. It is well known (see Pope 2000 for a summary) that the flat-plate laminar boundary layer undergoes transition to the TBL at a Reynolds number of order $Re_\theta \sim 800$, and that this value can vary strongly with type of flow disturbance (the problem of receptivity).

There have been many classic experiments on both the low- and high-Reynolds-number TBL varying from low, near transition (Erm & Joubert 1991), to large, laboratory-scale Reynolds numbers (Klebanoff 1954; Österlund 1999; DeGraaff & Eaton 2000; Hutchins & Marusic 2007*b*; and others), to huge values with von Kármán number $Re_\tau \approx 10^6$ (Metzger *et al.* 2007), typical of atmospheric surface layer TBLs. Direct numerical simulation of the Navier–Stokes equations has reached a stage of development where the TBLs at the lower end of the Re_θ range, of order $Re_\theta \approx 1000$–2900 have been successfully performed for both the transition (Moin 2009) and the fully developed TBL case (Spalart 1988; Spalart, Moser & Rogers 1991; Ferrante & Elghobashi 2004, 2005; Simens *et al.* 2009; Araya *et al.* 2011). See Schlatter & Örlü (2010) for an interesting compilation of recent DNS results.

The DNS studies have addressed several important issues for the numerical simulation of the TBL including high-order non-spectral methods and boundary conditions suitable for spatially developing flows with only one, as opposed to two, homogeneous directions. For the ZPGFPTBL it is necessary to provide realistic turbulence inflow properties as reviewed by Keating *et al.* (2004). Spalart (1988) proposed a systematic multiple-scale procedure to approximate the local effects of the streamwise growth of the flow. Using streamwise periodicity, Spalart (1988) performed DNS at Re_θ up to 1410. Lund, Wu & Squires (1998) (LWS) proposed a modification to Spalart's approach using a re-scaling technique. Here the inflow velocity is generated in a first simulation (code-A) and used in a second, TBL simulation (code-B). Code-A generates its own inflow conditions by rescaling the instantaneous velocity data of a downstream recycling plane, which are then re-introduced at the inlet; see figure 1 adapted from Simens *et al.* (2009). Inflow conditions for Code-B can then be taken directly from an interior plane of the code-A simulation. Inflow-generating methodology remains an area of active research (Keating *et al.* 2004; Liu & Pletcher 2006; Simens *et al.* 2009; Araya *et al.* 2011; Jewkes, Chung & Carpenter 2011), and we will later refer to 'code-A only' and 'code-A&B' methods. Simens *et al.* (2009) advocate a code-A only method (no code-B) restricting the re-scaling region to some

fraction of the total streamwise domain. Ferrante & Elghobashi (2004) performed DNS with $Re_\theta = 800$–1430 using an improved LWS, code-A&B approach by carefully prescribing, prior to rescaling, both the Reynolds stress tensor and the energy spectra in addition to the mean streamwise velocity when initializing the flow field of code-A.

4. Numerical method

4.1. *Spectral-finite-difference method*

A fourth-order numerical code has been implemented for LES (and some DNS) on a fully developed ZPGFPTBL flow. The governing equations are solved in a box with dimensions $L_x \times L_y \times L_z$, with periodic boundary condition in the spanwise or y-direction. The components of the velocity vector $\boldsymbol{u}$ are u, v and w in the streamwise (x-), spanwise (y-) and wall-normal (z-) directions respectively. The fractional step, or time-splitting method is implemented in terms of an approximated LU decomposition (Perot 1993) and the low-storage third-order semi-implicit Runge–Kutta method of Spalart *et al.* (1991) is used for temporal discretization. The implicit treatment of viscous terms allows large time steps to be taken in general. Only the viscous terms in the z-direction are treated implicitly, and the nonlinear and wall-parallel viscous terms are treated explicitly. The CFL number is order unity. Explicit, fourth-order finite differences on a staggered grid are used to approximate (x, z)-derivatives, while a Fourier spectral method is utilized for y-derivatives. The convective terms are calculated using a fully conservative skew-symmetric form (Morinishi *et al.* 1998). Nonlinear terms are treated using a pseudo-spectral method with a p_1th-order Fourier exponential filter, which mimics the 2/3 rule, in order to prevent aliasing errors (Gottlieb & Shu 1997; Chung & Pullin 2009). The Poisson-pressure equation, which reduces to a set of two-dimensional Helmholtz equations owing to the Fourier expansion in the spanwise (y-) direction, is solved using a cosine transform in the streamwise (x-) direction and a septa-diagonal matrix solver (available from LAPACK) in the wall-normal (z-) direction. This leads to efficient code parallelization. At boundaries, a ghost point scheme is employed where points are extended beyond boundaries so that a consistent stencil can be used as in the interior. This is, in effect, equivalent to a one-sided, finite-difference scheme at wall boundaries. Values at ghost points are designed to ensure global conservation of mass and momentum. The formulation in part follows Morinishi *et al.* (1998). Inflow-boundary conditions suitable for the fully developed ZPGFPTBL have been implemented for LES as described below.

For the fully developed ZPGFPTBL a code-A only, recycling flow method shown in figure 1, is used for the LES. For inflow we use the method of Lund *et al.* (1998). Briefly, the velocity data at a downstream location, referred to as the 'recycling plane' (figure 1), is rescaled to account for the growth of the thickness of the boundary layer in the x-direction. It is then re-introduced at the inlet of the computational domain. The velocity is decomposed into a mean and fluctuating part and the appropriate empirical similarity scaling laws are then applied to each component separately. The rescaling technique is based on the assumption that the velocity profile at both the recycling and inlet planes satisfy the similarity law of the boundary layer, namely, the law of the wall in the inner part and the defect law in the outer part. Also u_τ (we actually use η_0) at the inlet is estimated by the scaling relationship

$$u_{\tau,inlet} = u_{\tau,recycle}(\theta_{recycle}/\theta_{inlet})^{1/[2(n-1)]}, \tag{4.1}$$

which can be derived using a standard power-law approximation, here with $n = 7$. The recycling plane is generally at $0.8\,L_x$ although, as discussed below, other values are also used.

4.2. *Boundary conditions*

A convective boundary condition at the outflow boundary has been implemented of the form $\partial \boldsymbol{u}/\partial t + U_c(z)\partial \boldsymbol{u}/\partial x = 0$, where $U_c(z)$ is the local mean streamwise velocity at the exit. At the upper/free-stream boundary we use Dirichlet conditions for both u and p and a stress-free condition for the velocity component v; $u = U_\infty, \partial v/\partial z = 0, p = 0$ at $z = L_z$. The wall-normal velocity w is free to adjust to the solution (Simens 2008). Alternative boundary conditions are stress-free conditions for u and v and a Dirichlet condition for w; $w = W(x), \partial u/\partial z = \partial v/\partial z = 0$ at $z = L_z$, where the prescribed suction-blowing distribution of $W(x) = U_\infty\, \mathrm{d}\delta^*/\mathrm{d}x$ controls the pressure gradient. Here, δ^* is the boundary layer displacement thickness and U_∞ is the free-stream velocity. Simens *et al.* (2009) used the known experimental growth rate of δ^*. An alternative is that this can be computed from the mean velocity field (Lund *et al.* 1998). Other choices for the upper boundary could be used, for example a zero-vorticity condition. Fasel (1976) pointed out that a zero-vorticity condition at the top boundary needs a relatively small integration domain in the wall-normal direction. This becomes useful for the transition boundary layer (Moin 2009) since prescribing w at the top of the domain using the Blasius solution is a good choice in that case.

4.3. *Verification*

This code, with streamwise periodic boundary conditions, has been tested in DNS of channel flow at $Re_\tau = 187$ (Kim, Moin & Moser 1987) and also for LES of channel flow at $Re_\tau = 2 \times 10^3$–2×10^6 (not shown). The implementation of non-periodic boundary conditions has been tested for the growth of laminar boundary layers, where results compare well with the Blasius solution (not shown), and also for 256^3 DNS of the ZPGFPTBL at moderate Re_θ. Results for $Re_\theta = 666$ are shown in figure 2 in comparison with Spalart (1988).

The present code is highly optimized for parallel simulation of the boundary layer flow, and the overhead for the implementation of the stretched-vortex model, including the wall model, is of order 80 % when the model is implemented at every grid point. This includes solving a cubic analytically for the eigenvector directions, the structure function calculations per grid point, the calculation of the SGS kinetic energy and the SGS stresses and the solution of the wall-model ODEs. In practice the SGS model is switched off in the free stream and so the total SGS overhead is of order 30 %–40 %. While this is not small it will be seen that the LES can be run with uniform grids, with no near-wall refinement required, to essentially arbitrarily large Reynolds number, and at a cost independent of Reynolds number. The implementation of both the interior SGS model and the wall model are local.

5. LES of the zero-pressure-gradient turbulent boundary layer

5.1. *Range of LES performed*

The near-wall SGS model was implemented for the purpose of performing LES of the ZPGFPTBL over a range of Re_θ. Equation (2.10) was solved by the same third-order Runge–Kutta scheme as the main part of the flow simulation. Large-eddy simulations have been performed at several different resolutions (N_x, N_y, N_z) and for several domain sizes ($L_x/\delta_0, L_y/\delta_0, L_z/\delta_0$) summarized in table 1. For all LES the grid size in

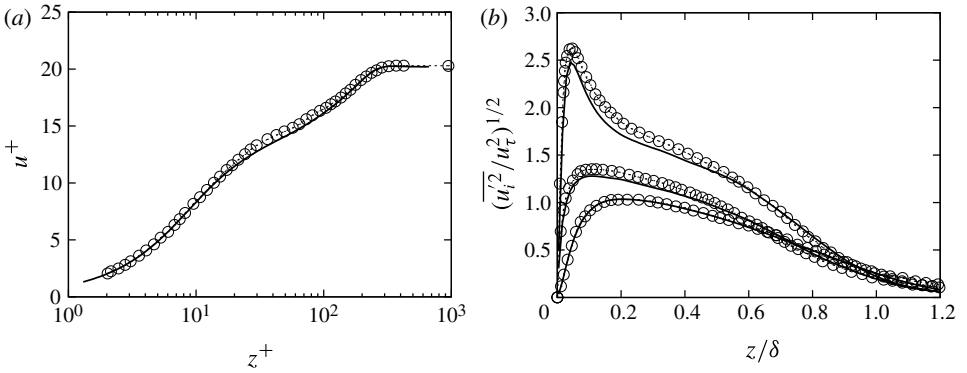

FIGURE 2. Comparison of present results with DNS. (*a*) Mean velocity profiles u/u_τ, (*b*) root-mean-square fluctuations. δ is the local 99 % boundary layer thickness; ∘, Spalart (1988) at $Re_\theta = 670$; solid lines, current code at $Re_\theta = 666$.

Case	Re_0	L_x/δ_0	L_y/δ_0	L_z/δ_0	N_x	N_y	N_z	h_0/δ_0	x_{ref}/L_x
A1–A20	16k −10T	36	6	4	384	64	128	5.6×10^{-3}	80 %
A4L	200k	36	6	4	192	32	64	1.1×10^{-3}	80 %
A4H	200k	36	6	4	768	128	256	2.8×10^{-3}	80 %
A16L	100G	36	6	4	192	32	64	1.1×10^{-3}	80 %
A16H	100G	36	6	4	768	128	256	2.8×10^{-3}	80 %
B4	200k	72	6	4	768	64	128	5.6×10^{-3}	40 %
B4a*	200k	72	6	4	768	64	128	5.6×10^{-3}	40 %
B4b	200k	72	6	4	768	64	128	5.6×10^{-3}	80 %
B16	100G	72	6	4	768	64	128	5.6×10^{-3}	40 %
B18	1T	72	6	4	768	64	128	5.6×10^{-3}	40 %
C16	100G	144	6	4	1536	64	128	5.6×10^{-3}	20 %
C18	1T	144	6	4	1536	64	128	5.6×10^{-3}	20 %

TABLE 1. Simulation parameters: $k \equiv 10^3$, $M \equiv 10^6$, $G \equiv 10^9$, $T \equiv 10^{12}$; $Re_0 = U_\infty \delta_0/\nu$; U_∞ is the free-stream velocity, δ_0 is the 99 % boundary layer thickness at the inlet of the domain. $\Delta_x = \Delta_y = 3\Delta_z$. $h_0 = 0.18\Delta_z$. Re_0 for each case A: A1, 16k; A2, 64k; A3, 160k; A4, 200k; A5, 640k; A6, 1M; A7, 4M; A8, 10M; A9, 40M; A10, 100M; A11, 400M; A12, 1G; A13, 4G; A14, 10G; A15, 40G; A16, 100G; A17, 400G; A18, 1T; A19, 4T; A20, 10T. * The mirroring method is employed for inflow generation scheme.

each direction was uniform with no stretching in the wall-normal direction. In total the results of some 31 different simulations are reported here in detail, and additional simulations are also mentioned briefly. Typically an individual LES is done by fixing a nominal Reynolds number $Re_0 = U_\infty \delta_0/\nu$, where δ_0 is the inlet boundary layer thickness. This will then span a range of Reynolds number Re_θ, which is an output of the LES. The parameter $x_{\rm ref}/L_x$ gives the position of the recycling plane as a fraction of the streamwise domain L_x, and it is noted that two different values were used with little effect on the present results shown. The inflow generation scheme of Lund *et al.* (1998) was used for all LES except for case B4a, where the mirroring method proposed by Jewkes *et al.* (2011) was implemented. This will be discussed below.

Case	N_x, N_y, N_z	Re_θ	U_e^+	$\overline{\mathscr{K}_1}$	H
A4L	192, 32, 64	2.53×10^4	30.4	0.382	1.30
A4	384, 64, 128	2.51×10^4	30.2	0.387	1.27
A4H	768, 128, 256	2.51×10^4	30.2	0.397	1.27
Experiment	n/a	2.58×10^4	30.5	0.384	1.30
A16L	192, 32, 64	6.13×10^9	61.4	0.371	1.18
A16	384, 64, 128	6.12×10^9	61.5	0.371	1.14
A16H	768, 128, 256	6.12×10^9	61.8	0.370	1.12

TABLE 2. Effect of resolution. Domain size fixed to $(L_x/\delta_0, L_y/\delta_0, L_z/\delta_0) = (36, 6, 4)$. Experimental data: Österlund (1999), $Re_\theta = 25767.5$. Data are taken at $x/\delta_0 \approx 28$.

Some physical parameters of interest are the displacement and momentum thicknesses δ^* and θ respectively and the Rotta–Clauser length scale $\Delta \equiv U_e^+ \delta^*$, where U_e^+ and the skin-friction coefficient C_f are given by

$$U_e^+ \equiv \frac{U_\infty}{u_\tau} = \sqrt{\frac{2}{C_f}}, \quad C_f \equiv \frac{\tau_w}{\frac{1}{2}\rho U_\infty^2}. \tag{5.1}$$

All results shown here are obtained as spanwise/time averages as a function of streamwise distance. Owing to the large range of Re_θ explored, LES results were obtained using many different Re_0. In what follows we will distinguish between our SGS/LES estimate of the von Kármán constant $\mathscr{K}_1$ and experimental estimates, which will be denoted by κ.

5.2. *Effect of resolution and domain length*

The effect of LES resolution at $Re_\theta \approx 2.5 \times 10^4$ from case A4, A4L and A4H, is shown in figures 3 and 4 respectively and also in table 2, which also shows the effect of resolution using cases A16, A16L and A16H at $Re_0 = 100G$. For each of the three resolutions $h_0/\Delta_z = 0.18$ is fixed, so that h_0/δ_{99} reduces with increasing resolution. In figure 3(*a*) the plots of U_e^+ versus Re_θ show a hill or bump after the inlet, also seen in DNS studies (Simens *et al.* 2009), which is perhaps the effect of non-equilibrium following inlet as a result of the recycling procedure with fixed $n = 7$ in (4.1). The wall-normal profiles discussed below were almost always downstream of the hill. Further, apart from the small rise in U_e^+, we find negligible effect when wall-normal profiles are plotted as a function of streamwise distance down the whole simulation domain for a given LES. A dynamic recycling method that eliminates the need for (4.1) has been proposed by Araya *et al.* (2011), which may alleviate this effect, and which may allow shorter domain sizes in both DNS and LES of spatially developing boundary layer flows. This has not been used here.

Comparisons are also made in figure 3(*a*) with the experiments of Österlund (1999). The lowest-resolution LES contains only 15–20 points in the turbulent boundary layer but still captures the skin friction characterized as U_e^+, the shape factor H and the mean velocity profile reasonably accurately. Table 2 shows only a small variation in the calculated von Kármán constant with different resolution, at each of the two Re_θ.

It can be seen in figure 3(*b*) that there is a drop-off in u^+ towards the virtual wall. We interpret this as the influence of a near-wall length scale of order the cell size as analysed by Brasseur & Wei (2010). They argue that this is a logarithmic-layer

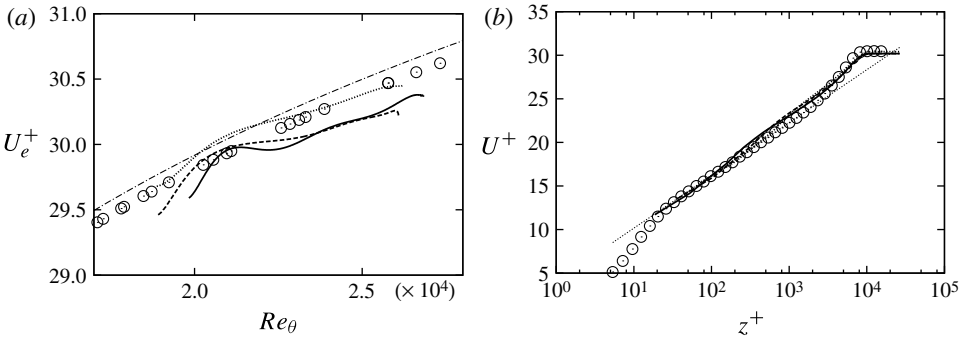

FIGURE 3. (*a*) U_e^+ versus Re_θ and Coles–Fernholz 2 (Nagib, Chauhan & Monkewitz 2007). (*b*) Mean streamwise velocity $u^+ \equiv \overline{u}/u_\tau$ and a log relationship with $\kappa = 0.384$ and $B = 4.127$ suggested by the experiment of Österlund (1999), $Re_\theta \approx 2.5 \times 10^4$. Open symbols, experiment (Österlund 1999). Lines, LES: dotted, lowest resolution ($192 \times 32 \times 64$) (case A4L); dashed, intermediate resolution ($384 \times 64 \times 128$) (case A4); solid, highest resolution ($764 \times 128 \times 256$) (case A4H).

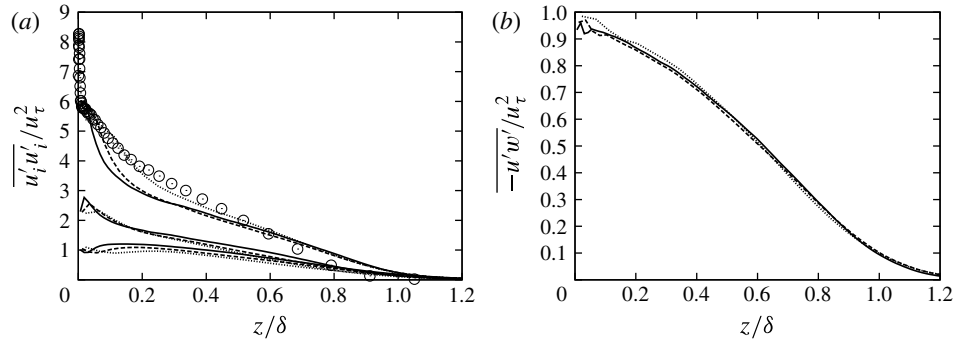

FIGURE 4. $Re_\theta \approx 2.5 \times 10^4$. (*a*) Streamwise (top), spanwise (middle) and wall-normal (bottom) intensities $\overline{u_i'^{2+}} \equiv \overline{u_i'^2}/u_\tau^2$. (*b*) Reynolds shear stresses $\overline{u'w'^+} \equiv \overline{u'w'}/u_\tau^2$. Open symbols, experiment at $Re_\theta = 2.0 \times 10^4$ (Marusic *et al.* 2010*a*). Lines, LES: dotted, lowest resolution ($192 \times 32 \times 64$) (case A4L); dashed, intermediate resolution ($384 \times 64 \times 128$) (case A4); solid, highest resolution ($764 \times 128 \times 256$) (case A4H). δ is the local 99 % boundary layer thickness.

mismatch and discuss in detail the simulation conditions under which this effect can be minimized by placing parameters into a domain referred to as the 'high-accuracy zone'. One condition, namely the number of points in the boundary layer of order 50–60, is approximately satisfied by our highest vertical resolution $N_z = 256$ (case A4H and A16H) but not by the wall-normal resolution $N_z = 128$ used in the majority of the present LES. While the Brasseur–Wei effect is certainly seen in the present LES, we remark that we do not obtain estimates of the von Kármán constant from the mean velocity profile but rather direct from the SGS model.

In figure 4(*a*,*b*), the streamwise turbulent intensities and the Reynolds stress contain SGS corrections to the resolved flow calculated as $\overline{u_i'u_j'} = \overline{\widetilde{u}_i'\widetilde{u}_j'} + \overline{T_{ij}}$. The higher-resolution LES results for the streamwise intensity $\overline{u_i'^{2+}}$ in figure 4(*a*) show a somewhat more flattened shape than the measurements of Marusic, Mathis & Hutchins

Case	L_x/δ_0	x_{ref}/δ_0	Re_θ	U_e^+	$\overline{\mathscr{K}_1}$	H
A4	36	28.8	2.51×10^4	30.2	0.388	1.27
B4	72	28.8	2.52×10^4	30.2	0.387	1.27
B4a	72	28.8	2.52×10^4	30.2	0.388	1.27
B4b	72	57.6	2.51×10^4	30.1	0.390	1.27

TABLE 3. Effect of domain size and the location of the recycling plane at $Re_\theta \approx 2.5 \times 10^4$. Data are taken at $x/\delta_0 \approx 28$.

(2010*a*), underestimating the experiment nearer the wall by up to 15 %. In figure 4(*b*), the Reynolds stress $\overline{u'w'^+}$ is essentially independent of resolution.

Some large-eddy simulations were also performed for a longer domain using the intermediate resolution (case Bs, Cs). Table 3 indicates that the effect of doubling the domain length in the streamwise direction on some of the principal parameters is small. A similar sensitivity on the mean velocity and turbulence intensity profiles (not shown) was also found. Longer domains are, however, expected to be required to better capture the dynamics of long structures of order 15–20 boundary layer thicknesses observed in the logarithmic region of the TBL (Kim & Adrian 1999; Hutchins & Marusic 2007*a*,*b*). This issue is not addressed here. In addition, many large-eddy simulations not reported here were performed to explore the effect of using both the code-A&B approach and the alternative, stress-free boundary conditions at the upper boundary. These variations did not produce LES results that were significantly different from those discussed below.

5.3. *Skin friction and H-factor*

Most of the large-eddy simulations discussed below were performed with our intermediate resolution and correspond to cases A1–A20 of table 1. Figures 5 and 6 plot the outer velocity normalized by the friction velocity U_e^+ over lower and higher ranges of Re_θ respectively. Also shown are experimental measurements (Österlund 1999), a compendium of results from DNS (see Schlatter & Örlü 2010) and the semi-empirical relation given by Nagib *et al.* (2007) as 'Coles–Fernholz 2':

$$\left(U_e^+\right)_{CF} = \frac{1}{\kappa}\log\left(Re_\theta\right) + C, \quad \kappa = 0.384, \quad C = 4.127. \tag{5.2}$$

In figure 5, U_e^+ at our lowest $Re_0 = 16 \times 10^3$ ($Re_\theta \approx 10^3$) agrees reasonably well with both experiment and DNS despite the fact that in this range our first grid point is inside or close to the viscous sublayer where our wall model in region II is probably least accurate. Across our whole Re_θ range Coles–Fernholz 2 gives a reasonable representation of our LES results, which can be considered predictions past the largest experimental value of figure 6, $Re_\theta = 4 \times 10^4$. We remark that the small but systematic discrepancy in U_e^+ between the present LES and experiment evident in figure 5 is in fact rather smaller than the spread in the Schlatter & Örlü (2010) compilation of DNS at somewhat lower Re_θ.

It is evident from figure 6 that for some LES with Re_θ greater than about 10^8, the slope of U_e^+ versus $\log Re_\theta$ does not appear continuous with LES at other Re_θ and does not match the slope of the Coles–Fernholz 2 curve. This effect can also be seen in the Schlatter & Örlü (2010) DNS compilation of figure 5. To investigate this, some large-eddy simulations at large Re_θ were done with longer domains (cases B16, C16,

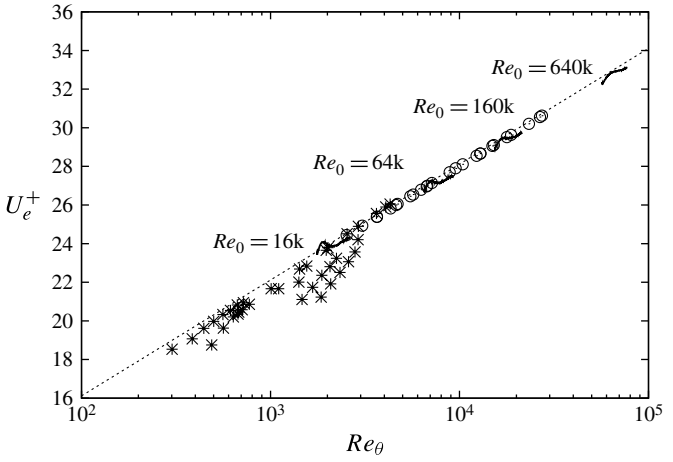

FIGURE 5. $U_e^+ \equiv U_\infty/u_\tau$ versus Re_θ up to $Re_\theta \approx 10^5$. Solid lines, current LES (cases A1–A3 and A5); ∘, experiment (Österlund 1999); ∗, DNS compilation (Schlatter & Örlü 2010); dashed line, Coles–Fernholz 2 (Nagib *et al.* 2007).

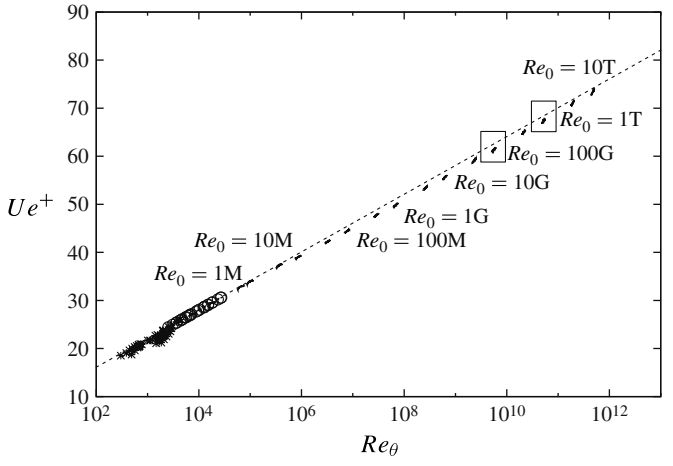

FIGURE 6. $U_e^+ \equiv U_\infty/u_\tau$ versus Re_θ up to $Re_\theta \approx 10^{12}$. Solid lines, current LES (cases; A1–A20); ∘, experiment (Österlund 1999); ∗, DNS compilation (Schlatter & Örlü 2010); dashed line, Coles–Fernholz 2 (Nagib *et al.* 2007).

B18 and C18) as indicated by the small boxes in figure 6. Some results are shown in figure 7 where it can be seen that substantially longer domains, up to $L_x = 144\delta_0$, appear to give an averaged slope consistent with the continuous curve of (5.2). We remark that the slope of the continuous function $U_e^+(Re_\theta)$ is Re_θ^{-1} times the slope of U_e^+ versus $\log[Re_\theta]$ shown in the graphs, so that the discrepancy refers to a function $U_e^+(Re_\theta)$ with slope magnitude $O(10^{-8}$–$10^{-12})$ over our large Re_θ range. In fact our maximum $Re_\theta = O(10^{12})$ is perhaps too large for practical applications but illustrates the capability of the present wall-bounded LES. At our largest Re_θ the kinematic viscosity ν is approaching machine roundoff error. We expect that even larger Re_θ could be achieved with quad-precision arithmetic.

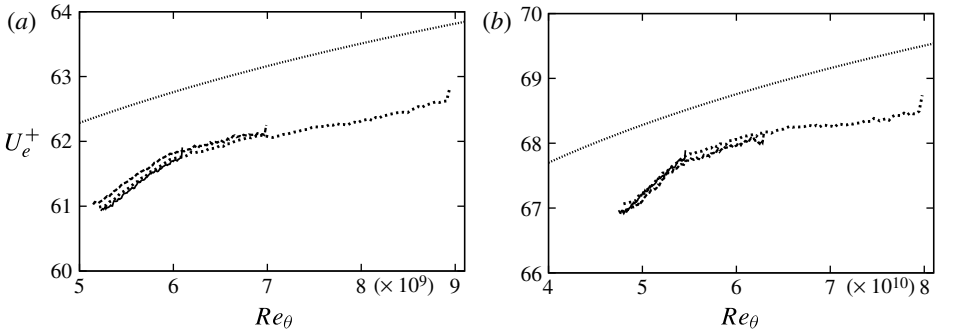

FIGURE 7. $U_e^+ \equiv U_\infty/u_\tau$ versus Re_θ with longer streamwise domains. (*a*) $Re_0 = 100$G, cases A16, B16 and C16. (*b*) $Re_0 = 1$ T, cases A18, B18 and C18. Solid lines, $L_x/\delta_0 = 36$ (A16, A18); dashed lines, $L_x/\delta_0 = 72$ (B16, B18), doted lines; $L_x/\delta_0 = 144$ (C16, C18), thin dashed-lines; Coles–Fernholz 2 (Nagib *et al.* 2007).

In addition to the A1–A20 LES at $(N_x, N_y, N_z) = (384, 64, 128)$, a set of 20 simulations were done over the full Re_θ range of figure 6 but at our lower resolution $(N_x, N_y, N_z) = (192, 32, 64)$. While these are not reported here in detail, we comment that these simulations showed comparison with each matching A1–A20 LES similar to that depicted in figures 3 and 4, and in table 2.

Nagib *et al.* (2007) obtain a large Re_θ, $H - Re_\theta$ relation by combining the exact result

$$H = \frac{1}{1 - (C'/U_e^+)}, \quad C' = \int_0^\infty \left(U_e^+ - u^+(z)\right)^2 \mathrm{d}\left(\frac{z}{\Delta}\right), \tag{5.3}$$

with the empirical approximation $C' = 7.135 + O(1/Re_\theta)$. This is shown in figure 8 compared with the Schlatter & Örlü (2010) DNS compendium and with the present LES. Also shown are 3 % deviation from (5.3). Given the dependence of the first of (5.3) on U_e^+, agreement between the LES and the asymptotic relation with the given C' is as expected. Nagib *et al.* (2007) point out that H does not appear to approach the traditional value $H = 1.3$ at large Re_θ. The shape factor may be viewed as the ratio of δ^*/δ_{99} to θ/δ_{99}, both of which decrease approximately as $1/\log(Re_\theta)$ when Re_θ increases. As the ratio of two small quantities, convergence in H from LES with increasing resolution can be expected to be slow at large Re_θ, and this is reflected in both table 2, where the effect of resolution on H is larger than for other tabulated quantities, and in figure 8. In particular the difference between case A16 and A16H is about 2 %, and it is clear that case A16H shows better agreement in both value and slope with the semi-empirical curve. The present LES may thus indicate approach to $H \to 1$ at gigantic Re_θ, but this is extremely slow.

5.4. *Mean velocity profiles and flow visualization*

Figure 9 shows mean velocity profiles in inner-scaling as $u^+ = \overline{u}(z^+)/u_\tau$ over a range of Re_θ. The log-relationship shown uses a value of the von Kármán constant $(\overline{\mathscr{K}_1})_{ave} = 0.378$ which is the average of the dynamic values obtained over cases A1–A20. It can be seen in figure 9 that there is a drop-off in u^+ near the virtual wall for the lower values of Re_θ. This is again the influence of a near-wall length scale of the order of the cell size as discussed by Brasseur & Wei (2010). This effect is weaker at our larger Re_θ. Figure 10 shows mean velocity defect profiles, $U_e^+ - u^+$,

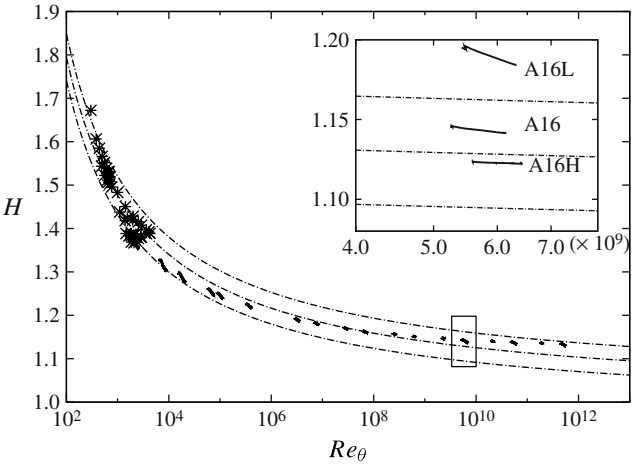

FIGURE 8. Shape factor $H = \delta^*/\theta$ versus Re_θ. Cases: A1–A20 and A16L, A16H shown in inner plot. Solid lines, current LES; $*$, DNS compilation (Schlatter & Örlü 2010); dashed line, (5.3) with 3 % error ranges (Nagib *et al.* 2007).

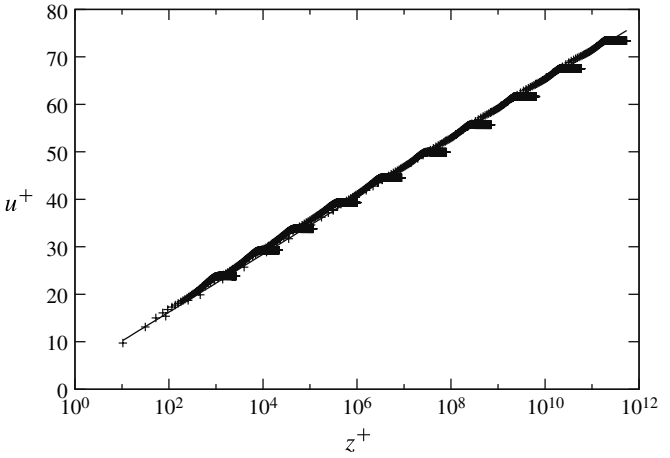

FIGURE 9. Mean velocity profiles $u^+ \equiv \overline{u}/u_\tau$ over a range of Re_θ taken at $x/\delta_0 \approx 24$. Cases: A1, A3, A6, A8, A10, A12, A14, A16, A18 and A20. Solid line, log relationship with $(\overline{\mathscr{K}_1})_{ave} = 0.378$, $B = 4.08$.

in the outer coordinates, indicating good collapse across the boundary layer. The profiles are in good agreement with that of DeGraaff & Eaton (2000) at $Re_\theta = 31\,000$. Taken together, figures 5–10 show that the wall model combined with the outer-scale LES captures the principal features of the ZPGFPTBL, in particular the wall-friction velocity u_τ and therefore the wall shear stress. This is despite the fact that both h_0^+ and the first LES point containing resolved-scale velocities, $h^+ = h_0^+ + \Delta_z^+/2$ for the staggered grid, may take extremely large values, for example $h_0^+ \approx 3 \times 10^9$ and $h^+ \approx 3 \times 10^{10}$ at $Re_\theta = O(10^{12})$. This could indicate that adequate modelling of the main physics of the log-layer is the key to successful LES of wall-bounded flows at very large Reynolds numbers.

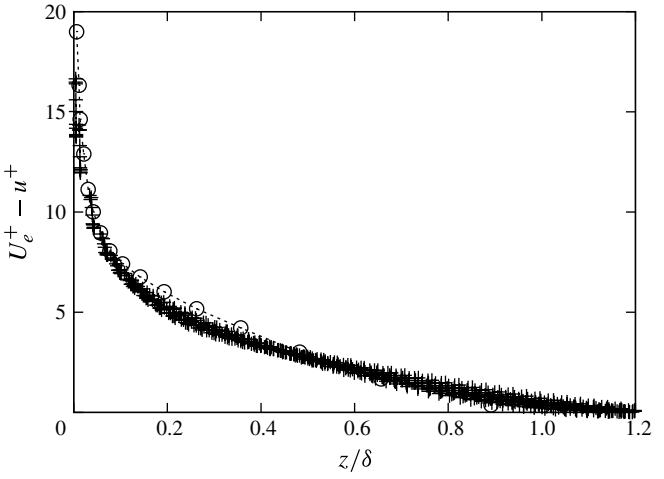

FIGURE 10. Mean velocity defect profiles over the same range of Re_θ as figure 9; ∘, experiment (DeGraaff & Eaton 2000).

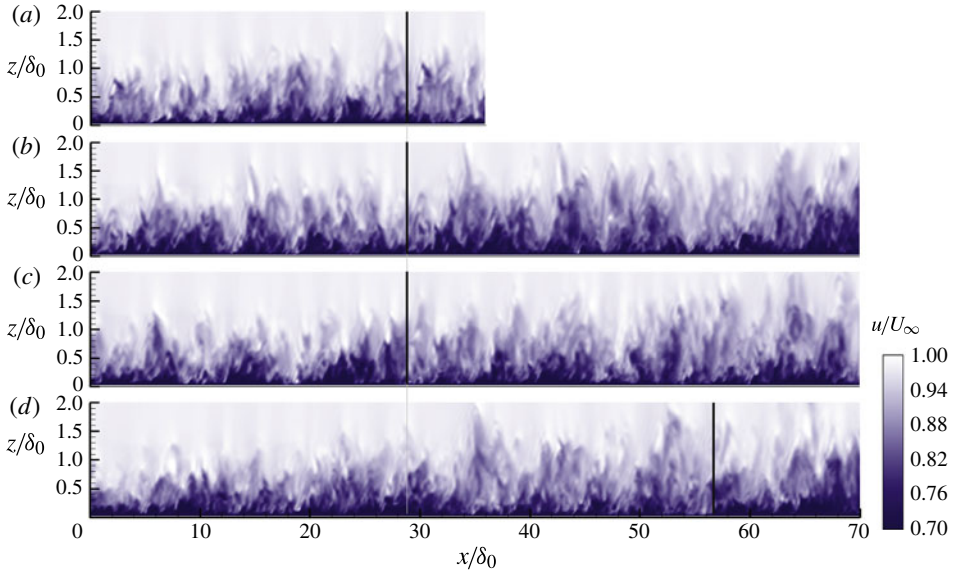

FIGURE 11. (Colour online available at journals.cambridge.org/flm) Contour plot of instantaneous streamwise velocity. Effect of x_{ref} position, domain size and inflow generation method. (*a*) Case A4, (*b*) case B4, (*c*) case B4a, (*d*) case B4b. The vertical solid lines indicate the position of recycling plane. $Re_\theta = 1.9$–2.6×10^4 (short domain), -3.3×10^4 (long domains). Note that case B4a uses a mirror-image recycling technique (Jewkes *et al.* 2011).

Figures 11–13 show contour plots of streamwise velocity, each plotted as u/U_∞ and each at a time instant during the particular LES indicated. The figures are not in proportion in x and z and each does not display the full domain height in the wall-normal direction. In figure 11(*a*,*b*) and perhaps (*c*) it can be observed that the large-scale structures at the inflow and after just downstream of the recycling plane

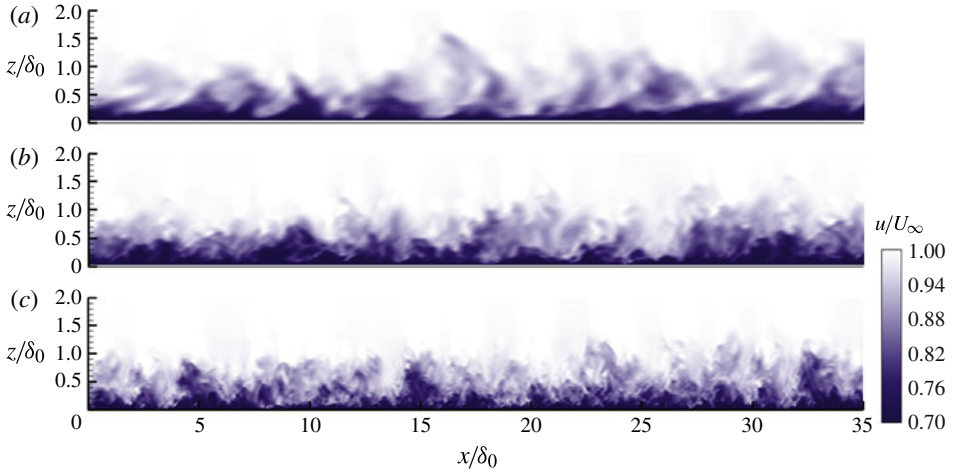

FIGURE 12. (Colour online) Contour plot of instantaneous streamwise velocity. Effect of resolution. (*a*) case A4L, (*b*) case A4, (*c*) case A4H. $Re_\theta = 1.9\text{–}2.6 \times 10^4$. These plots correspond to table 2.

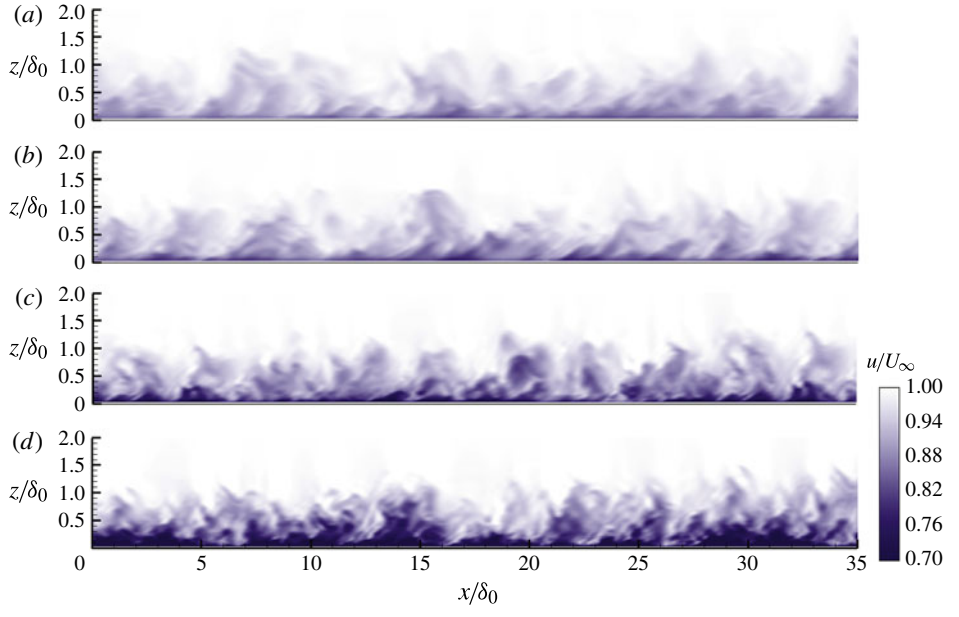

FIGURE 13. (Colour online) Contour plot of instantaneous streamwise velocity. Effect of Reynolds number. (*a*) A18, $Re_0 = 1T$, (*b*) A14, $Re_0 = 10G$, (*c*) A8, $Re_0 = 10M$, (*d*) A3, $Re_0 = 160k$. Range of Re_θ: A18, $4.8\text{–}5.6\times10^{10}$; A14, $5.6\text{–}6.8\times10^8$; A8, $7.5\text{–}9.8\times10^5$; A3, $1.5\text{–}2.1 \times 10^4$.

show some degree of correlation, suggesting quasi-periodic behaviour. For the LES case B4a shown in figure 11(*c*), the recycling technique of Jewkes *et al.* (2011) was used in which the inlet velocity field that is generated as a re-scaled version of the instantaneous velocity field at the recycling plane, is also subject to mirror-imaging about the wall-normal centreline of the inlet flow plane. This almost completely

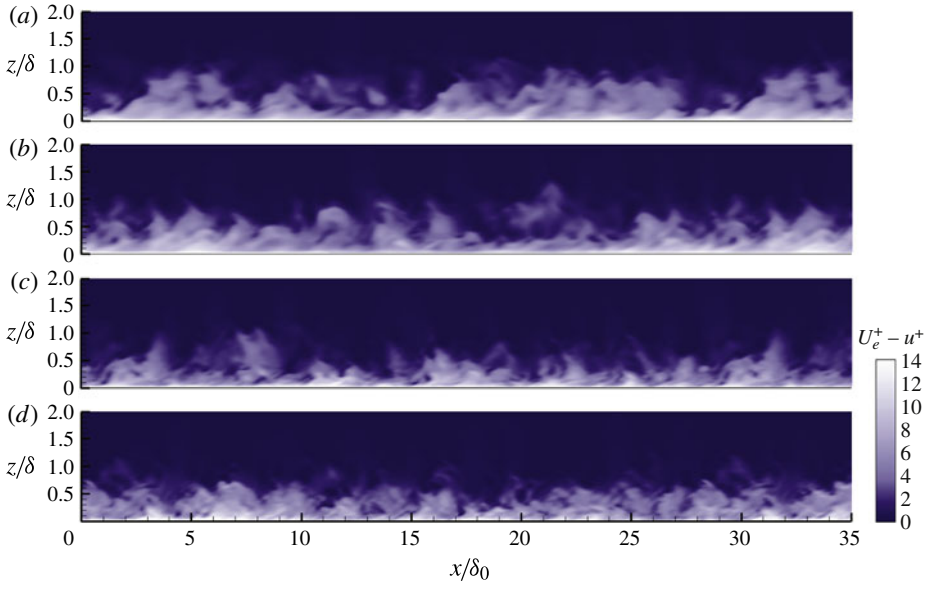

FIGURE 14. (Colour online) The contour plot of instantaneous velocity defect $U_e^+ - u^+$. Effect of Reynolds number. (*a*) A18: $Re_0 = 1T$, (*b*) A14: $Re_0 = 10G$, (*c*) A8: $Re_0 = 10M$ and (*d*) A3: $Re_0 = 160k$.

removes the spatially quasi-periodic effect in the overall LES. As shown in table 3 for $Re_\theta \approx 2.5 \times 10^4$, one-point statistics show almost no discernible effect from either the use or non-use of mirror imaging in the recycling method or the recycling domain length. This, however, may not be the case for two-point or other correlation statistics not discussed here.

Figure 12 shows the effect of resolution at $Re_\theta \approx 2.5 \times 10^4$. The three large-eddy simulations correspond to table 2 and to figures 3 and 4. The plots illustrate the dramatic effect of resolution in resolving turbulent scales, but the computed skin-friction and other parameters displayed in table 2 are little different for the three different resolutions. The effect of Reynolds number over a large range is shown in figure 13, where it is evident that, at a given distance from the wall as a fraction of the boundary layer thickness, the velocity fluctuations decrease. Contour plots of the instantaneous velocity defect $U_e^+ - u^+ \equiv (U_\infty - u)/u_\tau$ in an x–z plane are shown in figure 14. This corresponds to an instantaneous version of figure 10. It may be observed that, unlike figure 13, all four plots show somewhat similar colour coverage suggesting that fluctuations, as well as the mean of figure 10, show self-similarity in this scaling. There is, however, the impression that as Re_θ increases bottom to top in figure 14, the spatial scale of the fluctuation changes somewhat. This is probably the result of two effects, first that the contour plot shows only the resolved and not the subgrid velocity field, and second owing to the possible presence of long outer structures whose activity may be a function of Reynolds number. A study of the latter for the turbulent boundary layer is beyond the scope of the present work.

5.5. *Von Kármán 'constant' and the Coles wake factor*

The parameter $\mathscr{K}_1(x, y, t)$ defined in (2.12) can be interpreted as a Kármán-like constant. For plane channel flow Chung & Pullin (2009) found average values of

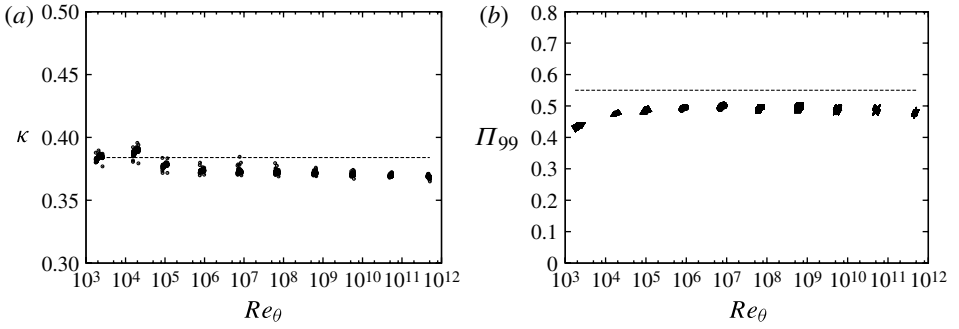

FIGURE 15. (*a*) Von Kármán 'constant' $\overline{\mathscr{K}_1}$ calculated dynamically. (*b*) Coles wake factor Π_{99}. Horizontal lines are recommended values by Nagib *et al.* (2007), $\kappa = 0.384$ and $\Pi_{99} = 0.55$ respectively. Cases shown are A1, A3, A6, A8, A10, A12, A14, A16, A18 and A20.

$(\overline{\mathscr{K}_1})_{\text{ave}} \approx 0.37$ broadly independent of Re_τ. The present variation of the spanwise/time-averaged values of $\mathscr{K}_1(x, y, t)$ as a function of Re_θ is depicted in figure 15(*a*) which show a weak dependence on Re_θ over many decades. The results appear as 'blobs' because each LES spans a range of Re_θ. We emphasize again that $\mathscr{K}_1(x, y, t)$ is calculated directly from the subgrid model near the wall and not from fitting a log-relationship to mean velocity profiles.

The Coles wake factor is an useful parameter characterizing the outer velocity profile. The wake parameter Π is defined from a universal profile fitted to the difference between the mean velocity and the logarithmic law (Coles 1956). Here we calculate Π_{99} using (Nagib *et al.* 2007)

$$u^+ = \frac{1}{\kappa}\log y^+ + B + \frac{\Pi}{\kappa}\mathscr{W}\left(\frac{y}{\delta}\right), \tag{5.4}$$

where δ is the boundary layer thickness and κ is the von Kármán constant. The function $\mathscr{W}(\xi)$ is a universal wake profile defined such that $\mathscr{W}(1) = 2$. We follow Nagib *et al.* (2007) and identify δ as the 99 % boundary layer thickness δ_{99} obtained from the spanwise/time-averaged mean velocity profile, approximate $\mathscr{W}(\delta_{99}/\delta) = 2$ and identify $\kappa = \overline{\mathscr{K}_1}$. Then a parameter Π_{99} can be calculated as

$$\Pi_{99} = \frac{\overline{\mathscr{K}_1}}{2}\left(0.99\,U_e^+ - \frac{1}{\overline{\mathscr{K}_1}}\log\delta_{99}^+ - B\right), \tag{5.5}$$

where, from (2.12), our effective value for B is

$$B = h_v^+ - \frac{\log h_v^+}{\overline{\mathscr{K}_1}}. \tag{5.6}$$

Values of Π_{99} calculated from the LES are shown in figure 15(*b*) plotted versus Re_θ. At our 'lower' Re_θ in the range 10^4–10^6 we find Π_{99} increases slowly, perhaps toward the asymptotic value $\Pi_{99} = 0.55$ recommended by Nagib *et al.* (2007) while remaining just below the statistical scatter of the experimental results shown in their figure 8. At our larger Re_θ we find $\Pi_{99} \approx 0.5$ with a weak Re_θ dependence.

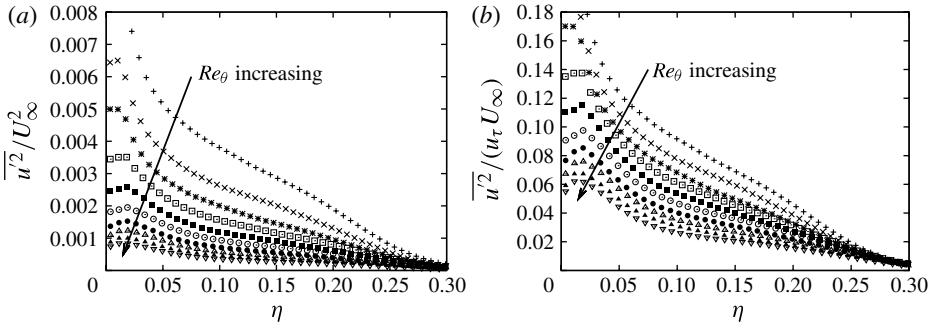

FIGURE 16. Streamwise velocity fluctuation. (*a*) Outer-scaling, $\overline{u'^2}/U_\infty^2$ versus $\eta \equiv z/\Delta$, (*b*) mixed scaling, $\overline{u'^2}/(U_\infty\, u_\tau)$ versus η. Arrows indicate increasing Re_θ. +, A1; ×, A3; ∗, A6; □, A8; ■, A10; ○. A12; •, A14; △, A16; ▲, A18; ▽, A20. Data are taken at $x/\delta_0 \approx 24$ for each case.

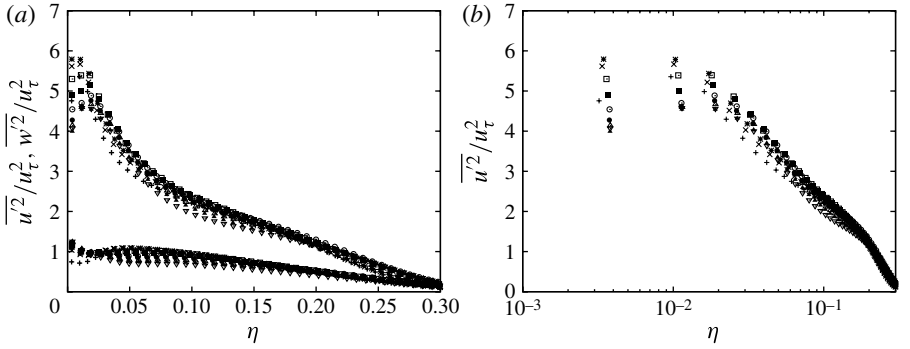

FIGURE 17. Streamwise and wall-normal velocity fluctuation. (*a*) Inner-scaling, $\overline{u'^2}/u_\tau^2$ and $\overline{w'^2}/u_\tau^2$ versus $\eta \equiv z/\Delta$, (*b*) $\overline{u'^2}/u_\tau^2$ in linear-log co-ordinates. Symbols for streamwise velocity fluctuation are as in figure 16.

5.6. *Turbulence intensity profiles*

The turbulence intensity profiles for $u'^2 \equiv \overline{u'^2}$ with three different scalings are shown in figures 16 and 17 plotted against $\eta = z/\Delta$, where Δ is the Rotta–Clauser parameter. Figure 17 also shows $w'^2 \equiv \overline{w'^2}$ with inner-scaling. It seems clear that neither outer-scaling (figure 16*a*) nor mixed scaling (figure 16*b*) provide satisfactory collapse. Inner-scaling, however, provides reasonable collapse for both turbulence intensities across almost the whole plotted range of η in figure 17. The collapse is not as good over the two grid points nearest the wall and we interpret this as a near-wall effect of the composite LES wall model.

The outer collapse is consistent with a similarity model for the streamwise turbulence intensity in the ZPGFPTBL (Marusic, Uddin & Perry 1997; Marusic & Kunkel 2003). This model takes the form $u'^2/u_\tau^2 = F(z^+, Re_\tau)$, where $Re_\tau = \delta\, u_\infty/\nu$ is the von Kármán number and δ, interpreted here as $\delta = \delta_{99}$, is the boundary layer thickness. This is related to Δ as $\Delta/\delta = H\, Re_\theta/Re_\tau$, which ratio is nearly constant as a function of Re_θ (not shown here). In the outer part of the boundary layer the model becomes asymptotic to $u'^2/u_\tau^2 \sim -\log(z/\delta) \sim -\log(z/\Delta)$, consistent with the

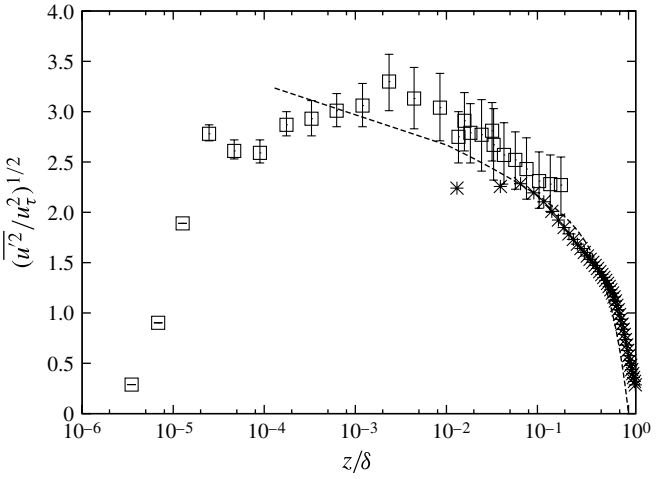

FIGURE 18. Streamwise root-mean-square fluctuation. $*$, case A9: $Re_0 = 40M$ at $Re_\tau = 1.1 \times 10^6$ ($Re_\theta = 3.4 \times 10^6$). $\boxminus$ with error bar, SLTEST data at $Re_\tau = 7.8 \times 10^5$ (Metzger *et al.* 2007). Dashed line, similarity model (Marusic *et al.* 1997; Marusic & Kunkel 2003).

outer-scaling suggested by the present LES. In figure 17(*b*) the LES collapse for $\overline{u'^2}/u_\tau^2$ is somewhat steeper than $-\log(z/\Delta)$. A specific comparison is shown in figure 18 at the LES $Re_\tau = 1.1 \times 10^6$. Except for the two LES grid-points nearest the wall, the LES and the full similarity model show reasonable agreement. Also shown are data from the Surface Layer Turbulence and Environmental Science Test (SLTEST) site in the western desert of Utah (Metzger *et al.* 2007). The LES results fall within the error bars of the data over most of the region of overlap save the two nearest wall points.

6. Discussion

Experimental and semi-empirical, asymptotic scenarios for high-Reynolds number wall-bounded flows (Monkewitz, Chauhan & Nagib 2007; Nagib *et al.* 2007; Marusic *et al.* 2010*b*) appear to provide a reasonable representation of the present LES predictions of the skin-friction and shape factor at extremely large Reynolds numbers. For the mean velocity profile, the present LES reveals no self-similar state at very large Re_θ: two length scales, ν/u_τ and δ, and two velocity scales, u_τ and U_∞, are always required to describe the streamwise velocity profile. Even though there exist quantitative discrepancies compared to experiment for the streamwise turbulence intensity (figure 4*a*), one-point, second-order turbulence statistics obtained from the LES nonetheless appear to collapse reasonably over almost all of the boundary layer thickness δ represented in the LES on one velocity scale, u_τ, and one length scale either δ or the Rotta–Clauser parameter Δ. This collapse, however, is not expected to be valid very near the wall, perhaps $z/\Delta < 0.01$, which is inaccessible to the present LES.

This last result has interesting implications for what is traditionally viewed as the smooth-wall ZPGFPTBL. Consider $Re_\theta \to \infty$ in each of three conceptual limits: (i) the streamwise distance x and U_∞ are fixed and $\nu \to 0$, (ii) $x \to \infty$ while U_∞ and ν are fixed, (iii) x and ν are fixed while $U_\infty \to \infty$ but the flow remains incompressible. Assuming that the LES trend, that turbulence intensities over the outer boundary layer scale on u_τ, continues for $Re_\theta > 10^{12}$, then since $1/U_e^+$ decreases monotonically,

this indicates that the turbulence intensity as a fraction of U_∞ expires in the limit $Re_\theta \to \infty$ over almost all the boundary layer. In other words, the outer part of the smooth-wall ZPGFPTBL asymptotically relaminarizes at sufficiently large Re_θ. This is consistent with the similarity model, where it can be shown that the wall-normal integral of (8) of Marusic *et al.* (1997), expressed as the the average u'^2/u_τ^2 over the boundary layer thickness, approaches a finite value when $Re_\tau \to \infty$.

The preceding discussion does not include the effect of the near-wall peak in u' and a possible second outer peak. While there is some evidence for the presence of a second or outer peak, for example in the SLTEST data shown in figure 18 and in super-pipe experimental data (Morrison *et al.* 2004), its wall-normal position appears to be a decreasing fraction of δ with increasing Reynolds number. For pipe flow Morrison *et al.* (2004) find $r_p/R \sim Re_\tau^{-1/2}$, where R_τ is the von Kármán number based on the pipe radius R. The inner peak appears to remain within the buffer layer at $z^+ \sim 15$. Two estimates for the magnitude of the inner peak are $u'_{max}/u_\tau = 1.86 + 0.12 \log Re_\theta$ (Metzger & Klewicki 2001) and $(u'_{max}/u_\tau)^2 = 4.84 + 0.467 \log Re_\tau$ (Hutchins *et al.* 2009) (natural logs). If one uses (5.2), then the first of these gives $u'_{max}/U_\infty \to 0.047$, $Re_\theta \to \infty$. If it is further assumed that $\Delta/(H\delta)$ approaches a finite limit when $Re_\theta \to \infty$, then the second expression, together with (5.2), gives $u'_{max}/U_\infty \to 1/(\log Re_\theta)^{1/2}$ and is asymptotically zero.

The above suggests two turbulent boundary layers. The first is an inner, near-wall layer containing one and perhaps two peaks in streamwise turbulence intensity, whose thickness is unknown but probably decreases as a fraction of δ when Re_θ increases. The second is an outer layer which is perhaps no more than the free-stream shadow of the inner layer, in which the turbulence decays asymptotically. This is consistent with the composite inner–outer model of Marusic & Kunkel (2003) and Marusic *et al.* (1997). The infinite Reynolds number limit would then be effective laminar slip flow, but perhaps with finite dissipation. This is strictly for the smooth-wall case with zero-pressure-gradient. The limits (i) and (iii) would be affected by surface roughness of a given length scale, but perhaps not the limit (ii), since $l^+ \equiv \nu/u_\tau$ increases with increasing x. For a strictly smooth wall, a straightforward calculation using (5.2) shows that the drag on a flat plate of length x is zero for limit (i) but unbounded for limits (ii) and (iii).

A further estimate of interest is the scaling of some norm $\|u'\|$ of the streamwise turbulence intensity with Re_θ. Again we consider a smooth wall (in the limit (ii) to avoid the effect of roughness) and will take a nominal norm $\| u' \| /u_\tau \approx 2.5$ as the streamwise turbulence intensity at 1 % boundary layer thickness suggested by figure 17. An alternative estimate based on an average over the whole boundary layer thickness could also be used (e.g. (8) of Marusic *et al.* 1997). This would affect the quantitative but not the qualitative character of the following argument. Again using the Nagib *et al.* (2007) expression (5.2) gives, together with $\| u' \| /u_\tau = 2.5$,

$$Re_\theta = 10^\beta, \quad \beta = 0.4343\,\kappa \left(\frac{2.5}{\| u' \| /U_\infty} - C \right), \tag{6.1}$$

for the value of Re_θ corresponding to a given boundary layer intensity norm $\| u' \| /U_\infty$. For $\| u' \| /U_\infty \approx 0.033$, (6.1) gives $Re_\theta \approx 10^{12}$. Assuming terrestrial conditions and $U_\infty = 40$ m s^{-1} in air at room temperature, this would require a plate length of about $10^{8.5}$ m at which station $\theta \approx 10^{4.7}$ m.

7. Concluding remarks

The present near-wall approach utilizes an integration across the wall-adjacent layer coupled to an analytical model for the LES slip velocity at a raised virtual wall, derived from the basic stretched-vortex SGS model. The model parameters are h_v^+, obtained empirically and h_0. The 'log law' (2.12) is obtained from the near-wall SGS ansatz with an assumption that attached SGS structures have sizes that scale with linear distance from the wall. At the scale of the boundary layer thickness, the wall model can be interpreted as essentially a variable-strength vortex sheet attached to the wall. The wall model describes the internal sheet structure in a way that provides its strength, or velocity jump, given by (2.12), which couples this structure to the outer-flow LES. We note that some parts of the composite wall model LES are independent of the stretched-vortex SGS model, for example (2.10) describing the wall-normal velocity gradient. This could be used combined with other SGS closures. Equation (2.12), however, is particular to the stretched-vortex model. The present LES ansatz follows that of Chung & Pullin (2009) for unidirectional flow. Vector versions of the wall model on a surface where the flow direction changes can easily be formulated starting from an integration across the two components of the wall-parallel momentum equation.

Our LES indicates that a moderately complex wall model is capable of capturing the principal features, including Reynolds number effects, of the smooth-wall, zero-pressure-gradient flat-plate turbulent boundary layer at essentially arbitrarily large Reynolds numbers and at cost independent of the Reynolds numbers. These large-eddy simulations are not perfect and display some near-wall effects associated with finite resolution and wall modelling. Large-eddy simulations at even larger Reynolds numbers appear viable but could need higher-precision arithmetic, at least for solving the auxiliary equation obtained from the wall-normal averaged, streamwise momentum equation. A useful feature of the model is that detailed resolution of the near-wall boundary layer is apparently not required to capture interesting flow properties such as the skin friction and the main features of the mean velocity profile in their dependence on Re_θ. The other side of the coin is that a possible disadvantage of our approach is that it provides no direct quantitative information on the near-wall region.

An interesting result of LES over a range of Reynolds number inaccessible to both present-day DNS and experiment is that, within the outer part of the turbulent boundary layer, the streamwise turbulence intensity scales with the wall-friction velocity u_τ and with neither the free-stream velocity U_∞ nor a mixed-scaling combination of u_τ and U_∞. While it cannot be ruled out that this is an artifact of the wall model, the agreement with surface layer data over the small region of overlap lends some support to this conclusion. The main parameters of LES are reasonably well described by well-known asymptotic models of the smooth-wall flat-plate boundary layer. In principle, however, our approach is not limited to this flow and can, with further development, be applied to flows with curvature, finite pressure gradients and roughness. These applications are left for future work.

This work has been supported in part by the National Science Foundation under Grant DMS-0714050. Helpful discussions with I. Marusic and B. McKeon are acknowledged.

REFERENCES

ANDERSON, A. & MENEVEAU, C. 2011 Dynamic roughness model for large-eddy simulation of turbulent flow over multiscale, fractal-like rough surfaces. *J. Fluid Mech.* **679**, 288–314.

ARAYA, G., CASTILLO, L., MENEVEAU, C. & JANSEN, K. 2011 A dynamic multi-scale approach for turbulent inflow boundary conditions in spatially developing flows. *J. Fluid Mech.* **670**, 581–605.

BRASSEUR, J. G. & WEI, T. 2010 Designing large-eddy simulation of the turbulent boundary layer to capture law-of-the-wall scaling. *Phys. Fluids* **22**, 021303.

CABOT, W. & MOIN, P. 1999 Approximate wall boundary conditions in the large-eddy simulation of high Reynolds number flow. *Flow Turbul. Combust.* **63**, 269–291.

CHUNG, D. & MCKEON, B. J. 2010 Large-eddy simulation of large-scale structures in long channel flow. *J. Fluid Mech.* **661**, 341–364.

CHUNG, D. & PULLIN, D. I. 2009 Large-eddy simulation and wall-modelling of turbulent channel flow. *J. Fluid Mech.* **631**, 281–309.

COLES, D. 1956 The law of the wake in the turbulent boundary layer. *J. Fluid Mech.* **1**, 191–226.

DEGRAAFF, D. B. & EATON, J. K. 2000 Reynolds-number scaling of the flat-plate turbulent boundary layer. *J. Fluid Mech.* **422**, 319–346.

ERM, L. P. & JOUBERT, P. N. 1991 Low-Reynolds-number turbulent boundary layers. *J. Fluid Mech.* **230**, 1–44.

FASEL, H. 1976 Investigation of the stability of boundary layers by a finite-difference model of the Navier–Stokes equations. *J. Fluid Mech.* **78**.

FERRANTE, A. & ELGHOBASHI, S. E. 2004 A robust method for generating inflow conditions for direct simulations of spatially-developing turbulent boundary layers. *J. Comput. Phys.* **198** (1), 372–387.

FERRANTE, A. & ELGHOBASHI, S. E. 2005 Reynolds number effect on drag reduction in a microbubble-laden spatially developing turbulent boundary layer. *J. Fluid Mech.* **543**, 93–106.

GOTTLIEB, D. & SHU, C. W. 1997 On the Gibbs phenomenon and its resolution. *SIAM Rev.* **39** (4), 644–668.

HEAD, M. R. & BANDYOPADHYAY, P. 1981 New aspects of turbulent boundary-layer structure. *J. Fluid Mech.* **107**, 297–338.

HUTCHINS, N. & MARUSIC, I. 2007*a* Evidence of very long meandering features in the logarithmic region of turbulent boundary layers. *J. Fluid Mech.* **579**, 1–28.

HUTCHINS, N. & MARUSIC, I. 2007*b* Large-scale influences in near-wall turbulence. *Phil. Trans. R. Soc.* A **365**, 647–664.

HUTCHINS, N., NICKELS, T. B., MARUSIC, I. & CHONG, M. S. 2009 Hot-wire spatial resolution issues in wall-bounded turbulence. *J. Fluid Mech.* **635**, 103–136.

JEWKES, J. W., CHUNG, Y. M. & CARPENTER, P. W. 2011 Modification to a turbulent inflow generation method for boundary-layer flows. *AIAA J.* **49** (1), 247–250.

JIMÉNEZ, J. 2003 Computing high Reynolds number turbulence: will simulations ever replace experiments? *J. Turbul.* **4**, 0227.

KEATING, A., PIOMELLI, U., BALARAS, E. & KALTENBACH, H. J. 2004 *A priori* and *a posteriori* tests of inflow conditions for large-eddy simulation. *Phys. Fluids* **16**, 4696.

KIM, K. C. & ADRIAN, R. J. 1999 Very large-scale motion in the outer layer. *Phys. Fluids* **11**, 417–422.

KIM, J., MOIN, P. & MOSER, R. 1987 Turbulence statistics in fully developed channel flow at low Reynolds number. *J. Fluid Mech.* **177** (1), 133–166.

KLEBANOFF, P. S. 1954 Characteristics of turbulence in a boundary layer with zero pressure gradient. *NACA TN 3178*.

LESIEUR, M. & METAIS, O. 1996 New trends in large-eddy simulations of turbulence. *Annu. Rev. Fluid Mech.* **28**, 45–82.

LIU, K. & PLETCHER, R. H. 2006 Inflow conditions for the large-eddy simulation of turbulent boundary layers: a dynamic recycling procedure. *J. Comput. Phys.* **219** (1).

LU, H. & PORTÉ-AGEL, F. 2010 A modulated gradient model for large-eddy simulation: application to a neutral atmospheric boundary layer. *Phys. Fluids* **22**, 015109.

LUND, T. S., WU, X. & SQUIRES, K. D. 1998 Generation of turbulent inflow data for spatially-developing boundary layer simulations. *J. Comput. Phys.* **140** (2), 233–258.

LUNDGREN, T. S. 1982 Strained spiral vortex model for turbulent fine structure. *Phys. Fluids* **25**, 2193–2203.

MARUSIC, I. & KUNKEL, G. J. 2003 Streamwise turbulence intensity formulation for flat-plate boundary layers. *Phys. Fluids* **15**, 2461.

MARUSIC, I., MATHIS, R. & HUTCHINS, N. 2010*a* Predictive model for wall-bounded turbulent flow. *Science* **329** (5988), 193.

MARUSIC, I., MCKEON, B. J., MONKEWITZ, P. A., NAGIB, H. M., SMITS, A. J. & SREENIVASAN, K. R. 2010*b* Wall-bounded turbulent flows at high Reynolds numbers: recent advances and key issues. *Phys. Fluids* **22**, 065103.

MARUSIC, I., UDDIN, A. K. M. & PERRY, A. E. 1997 Similarity law for the streamwise turbulence intensity in zero-pressure-gradient turbulent boundary layers. *Phys. Fluids* **9**, 3718.

MATHIS, R., HUTCHINS, N. & MARUSIC, I. 2009 Large-scale amplitude modulation of the small-scale structures in turbulent boundary layers. *J. Fluid Mech.* **628**, 311–337.

MENEVEAU, C. & KATZ, J. 2000 Scale-invariance and turbulence models for large-eddy simulation. *Annu. Rev. Fluid Mech.* **32**, 1–32.

METZGER, M. M. & KLEWICKI, J. C. 2001 A comparative study of near-wall turbulence in high and low Reynolds number boundary layers. *Phys. Fluids* **13**, 692–701.

METZGER, M., MCKEON, B. J. & HOLMES, H. 2007 The near-neutral atmospheric surface layer: turbulence and non-stationarity. *Phil. Trans. R. Soc.* A **365**, 859–876.

MISRA, A. & PULLIN, D. I. 1997 A vortex-based subgrid stress model for large-eddy simulation. *Phys. Fluids* **9**, 2443–2454.

MONKEWITZ, P. A., CHAUHAN, K. A. & NAGIB, H. M. 2007 Self-consistent high-Reynolds-number asymptotics for zero-pressure-gradient turbulent boundary layers. *Phys. Fluids* **19**, 115101.

MORINISHI, Y., LUND, T. S., VASILYEV, O. V. & MOIN, P. 1998 Fully conservative higher order finite difference schemes for incompressible flow. *J. Comput. Phys.* **143** (1), 90–124.

MORRISON, J. F., MCKEON, B. J., JIANG, W. & SMITS, A. J. 2004 Scaling of the streamwise velocity component in turbulent pipe flow. *J. Fluid Mech.* **508**, 99–131.

NAGIB, H. M., CHAUHAN, K. A. & MONKEWITZ, P. A. 2007 Approach to an asymptotic state for zero pressure gradient turbulent boundary layers. *Phil. Trans. R. Soc. A Math. Phys. Engng Sci.* **365** (1852), 755.

NICKELS, T. B., MARUSIC, I., HAFEZ, S., HUTCHINS, N. & CHONG, M. S. 2007 Some predictions of the attached eddy model for a high Reynolds number boundary layer. *Phil. Trans. R. Soc.* A **365**, 807–822.

O'GORMAN, P. A. & PULLIN, D. I. 2003 The velocity-scalar cross spectrum of stretched spiral vortices. *Phys. Fluids* **15**, 280–291.

ÖSTERLUND, J. M. 1999 Experimental studies of zero pressure-gradient turbulent boundary layer flow. PhD thesis, KTH, Mechanics.

PEROT, J. B. 1993 An analysis of the fractional step method. *J. Comput. Phys.* **108** (1), 51–58.

PIOMELLI, U. 2008 Wall-layer models for large-eddy simulation. *Prog. Aeronaut. Sci.* **44**, 437–446.

PIOMELLI, U. & BALARAS, E. 2002 Wall-layer models for large-eddy simulations. *Annu. Rev. Fluid Mech.* **34**, 349–374.

POPE, S. B. 2000 *Turbulent Flows*. Cambridge University Press.

POPE, S. B. 2004 Ten questions concerning the large-eddy simulation of turbulent flows. *New J. Phys.* **6**, 35.

PORTÉ-AGEL, F., MENEVEAU, C. & PARLANGE, M. C. 2000 A scale-dependent dynamic model for large-eddy simulation: application to a neutral atmospheric boundary layer. *J. Fluid Mech.* **415**, 261–284.

PULLIN, D. I. 2000 A vortex-based model for the subgrid flux of a passive scalar. *Phys. Fluids* **12**, 2311–2319.

PULLIN, D. I. & LUNDGREN, T. S. 2001 Axial motion and scalar transport in stretched spiral vortices. *Phys. Fluids* **13**, 2553–2563.

ROBINSON, S. K. 1991 Coherent motions in the turbulent boundary layer. *Annu. Rev. Fluid Mech.* **23**, 601–639.

SAGAUT, P. 2002 *Large-eddy Simulation for Incompressible Flow: An Introduction*. Springer.

SCHLATTER, P., LI, Q., BRETHOUWER, G., JOHANSSON, A. V. & HENNINGSON, D. S. 2010 Simulations of spatially evolving turbulent boundary layers up to $Re_\theta = 4300$. *Intl J. Heat Fluid Flow* **31** (3), 251–261.

SCHLATTER, P. & ÖRLÜ, R. 2010 Assessment of direct numerical simulation data of turbulent boundary layers. *J. Fluid Mech.* **659**, 116–126.

SIMENS, M. P. 2008 The study and control of wall-bounded flows. PhD thesis, Aeronautics, Universidad Politécnica de Madrid, http://oa.upm.es/1047/.

SIMENS, M. P., JIMÉNEZ, J., HOYAS, S. & MIZUNO, Y. 2009 A high-resolution code for turbulent boundary layers. *J. Comput. Phys.* **228** (11), 4218–4231.

SPALART, P. R 1988 Direct simulation of a turbulent boundary layer up to $Re_\theta = 1410$. *J. Fluid Mech.* **187**, 61.

SPALART, P. R., MOSER, R. D. & ROGERS, M. M. 1991 Spectral methods for the Navier–Stokes equations with one infinite and two periodic directions. *J. Comput. Phys.* **96** (2), 297–324.

TEMPLETON, J. A., MEDIC, G. & KALITZIN, G. 2005 An eddy-viscosity based near-wall treatment for coarse grid large-eddy simulation. *Phys. Fluids* **17**, 105101.

TEMPLETON, J. A., WANG, M. & MOIN, P. 2008 A predictive wall model for large-eddy simulation based on optimal control techniques. *Phys. Fluids* **20**, 065104.

TOWNSEND, A. A. 1976 *The Structure of Turbulent Shear Flow*, 2nd edn. Cambridge University Press.

VOELKL, T., PULLIN, D. I. & CHAN, D. C. 2000 A physical-space version of the stretched-vortex subgrid-stress model for large-eddy simulation. *Phys. Fluids* **12**, 1810–1825.

WANG, M. & MOIN, P. 2002 Dynamic wall modelling for large-eddy simulation of complex turbulent flows. *Phys. Fluids* **14**, 2043–2051.

WU, X. & MOIN, P. 2009 Direct numerical simulation of turbulence in a nominally zero-pressure-gradient flat-plate boundary layer. *J. Fluid Mech.* **630**, 5–41.